Ploidy shapes gemcitabine response through altered potency and delayed cell death

Vural Tagal[1], Tao Li[1], Rikhil Kumar[1], Pujan Shrestha[2], Xiaoqing Yu[4], Daria Miroshnychenko[1], Kayode Olumoyin[1], Andriy Marusyk[1], Mark Davies[3], Stuart Maudsley[1], Issam El-Naqa[1], Ana P. Gomes[1], Derek R. Duckett[1], Hyo S. Han[1], and Noemi Andor[1,*]

[1]*H. Lee Moffitt Cancer Center & Research Institute, Tampa, FL, USA*
[2]*Texas A&M University, College Station, TX, USA*
[3]*Department of Genetics and Oncology, Cardiff University, Cardiff, UK*
[4] *Department of Biostatistics and Bioinformatics, H Lee Moffitt Cancer Center and Research Institute, Tampa, FL, USA*

Abstract

Tumor ploidy is increasingly recognized as a determinant of therapeutic response, but the mechanisms by which ploidy shapes sensitivity to specific cytotoxic agents remain unclear. Here, we investigated the relationship between ploidy and gemcitabine response using pharmacogenomic reanalysis, isogenic cancer cell systems, live-cell imaging, intracellular pharmacokinetic/pharmacodynamic (PKPD) measurements, and mathematical modeling. Across public pharmacogenomic datasets, gemcitabine emerged as a low-ploidy-selective cytotoxic agent. In matched isogenic low- and high-ploidy cell systems, higher-ploidy cells were consistently less sensitive to gemcitabine across multiple lineages. Focused live-cell imaging and PKPD measurements in near-diploid and near-tetraploid SUM-159 cells showed that both states formed intracellular dFdCTP, but high-ploidy cells exhibited weaker and slower treatment responses, with delayed accumulation of cell death. To quantify these differences, we developed a delay-aware live/dead model driven by intracellular dFdCTP exposure. The best-fit model identified both reduced effective gemcitabine potency and a substantially longer delay from intracellular drug action to observed death in high-ploidy cells. Specifically, the inferred mean delay was approximately 17.5 hours in near-diploid cells versus 42.5 hours in near-tetraploid cells. The model also supported a thresholded, nonlinear, and ploidy-dependent mapping from administered gemcitabine dose to effective intracellular drug action. Together, these results establish ploidy as a determinant of both the magnitude and timing of gemcitabine response and provide a quantitative framework for linking intracellular drug exposure to delayed cytotoxic outcomes across ploidy states.

Introduction

Whole-genome doubling (WGD) can buffer the fitness costs of chromosome missegregation. Emerging evidence indicates that WGD-positive cancer cells tolerate loss-of-heterozygosity events better than near-diploid cells [1], a principle supported by subsequent computational and experimental analyses of ploidy-dependent copy-number fitness landscapes [1, 2]. Conversely, lower-ploidy cells have less copy-number redundancy, so the same chromosome-loss event is more likely to create a lethal dosage imbalance, p53-dependent arrest, or death in the subsequent G_1 phase [3–6]. Consistent with this model, our ALFA-K framework, which infers karyotype fitness landscapes from longitudinal single-cell chromosome-count data, showed that regions near the diploid state are more rugged than regions near the tetraploid state [7]. We recently extended this concept into a mechanistic modeling framework by introducing a ploidy-dependent post-missegregation survival function. When this function was inferred by jointly fitting longitudinal tumor-burden trajectories and terminal single-cell chromosome-number distributions from in vitro and in vivo studies, the model's ability to recapitulate both datasets was highly sensitive to the form of the survival function [**?**]. Together, these findings suggest that ploidy is a quantitative determinant of whether chromosome-segregation errors are lethal, tolerated, or converted into heritable karyotypic variation.

Many anticancer drugs elevate chromosome missegregation either directly, by disrupting mitosis, or indirectly, by generating replication and DNA-damage lesions that persist into mitosis. A ploidy-dependent survival framework predicts that near-diploid cells should be particularly vulnerable to CIN-inducing therapies, because missegregation events, especially chromosome-loss events, impose larger immediate fitness costs before genome doubling. Consistent with this prediction, analysis of breast cancer cell-line drug responses identified multiple mitotic spindle poisons, including paclitaxel, vinblastine, and vinorelbine, among the strongest ploidy-associated agents [8]. Surprisingly, gemcitabine showed the strongest association with ploidy in this analysis. Although gemcitabine is classically viewed as an S-phase antimetabolite, an independent human artificial chromosome loss assay showed that it is also a potent inducer of chromosome loss, ranking among the highest CIN-inducing drugs tested and increasing chromosome loss by approximately 35–45-fold [9]. Independent drug-sensitivity studies have also identified gemcitabine as a low-ploidy-selective compound [10]. These observations nominate gemcitabine as an unexpected but compelling candidate for testing whether ploidy modifies chemotherapy response.

Gemcitabine acts as a nucleoside analogue that inhibits ribonucleotide reductase, depletes dNTP pools, and induces severe DNA replication stress. Even mild replication stress can increase lagging DNA, most lagging-DNA lesions form micronuclei, and roughly half of lagging-DNA-derived micronuclei can contain whole or near-whole chromosomes [11]. High or sustained gemcitabine exposures can produce persistent S-phase arrest associated with cell killing, whereas lower or clinically relevant pulse exposures may allow cells to survive the initial S-phase insult, undergo prolonged S/G_2 delay, and only later either recover or progress toward lethal downstream fates [12]. Thus, gemcitabine provides a clinically relevant setting in which replication stress can be coupled to later chromosome-segregation defects.

Several well-established mechanisms of gemcitabine resistance reduce either the formation or the lethality of replication stress. Upstream pharmacologic mechanisms include reduced intracellular drug exposure or activation, through low hENT1/SLC29A1 or low dCK [13–15]; increased drug inactivation or dephosphorylation, through CDA or NT5C1A [16, 17]; and on-target metabolic rescue through upregulation of RRM1/RRM2, which restores dNTP availability and blunts gemcitabine-induced fork collapse [18–20]. In parallel, resistant cells can tolerate replication stress through stronger checkpoint and fork-protection programs, including ATR/CHK1/WEE1-, NEK9-, or CK2-dependent buffering, thereby delaying or preventing conversion of S-phase damage into lethal mitosis [21–24]. However, these canonical mechanisms primarily explain variation in intracellular drug burden, fork collapse, and checkpoint control. Whether baseline ploidy itself modifies gemcitabine response remains less well understood.

Here, we test whether ploidy state predicts gemcitabine sensitivity across isogenic cancer cell systems. We combine ploidy-shifted cancer cell models, gemcitabine response measurements, chromosome-segregation phenotyping, and mathematical modeling to determine whether differences in chromosome-number state are associated with altered vulnerability to gemcitabine-induced cytotoxicity.

Results

Cytotoxic and signaling-directed agents show opposing ploidy associations across cancers

To identify therapeutic classes associated with ploidy-dependent drug response, we integrated GDSC drug-sensitivity measurements with CellPassports ploidy estimates, classified compounds into broad functional categories, and tested for enrichment of ploidy-associated drugs within each category (Methods **??**).

Across cancers, cytotoxic agents were significantly enriched among compounds whose IC50 increased with ploidy in 8/24 cancer types, whereas the opposite pattern was observed in only one cancer type (p-value ≤ 0.01; Supplementary Table 1). In contrast, signaling-targeted agents were significantly enriched among compounds whose IC50 decreased with ploidy in 5/24 cancer types, whereas the reverse pattern was observed in only two cancer types (p-value ≤ 0.01; Supplementary Table 2). These results support a broad but non-universal trend linking lower ploidy to cytotoxic vulnerability and higher ploidy to relative sensitivity to signaling-targeted therapies.

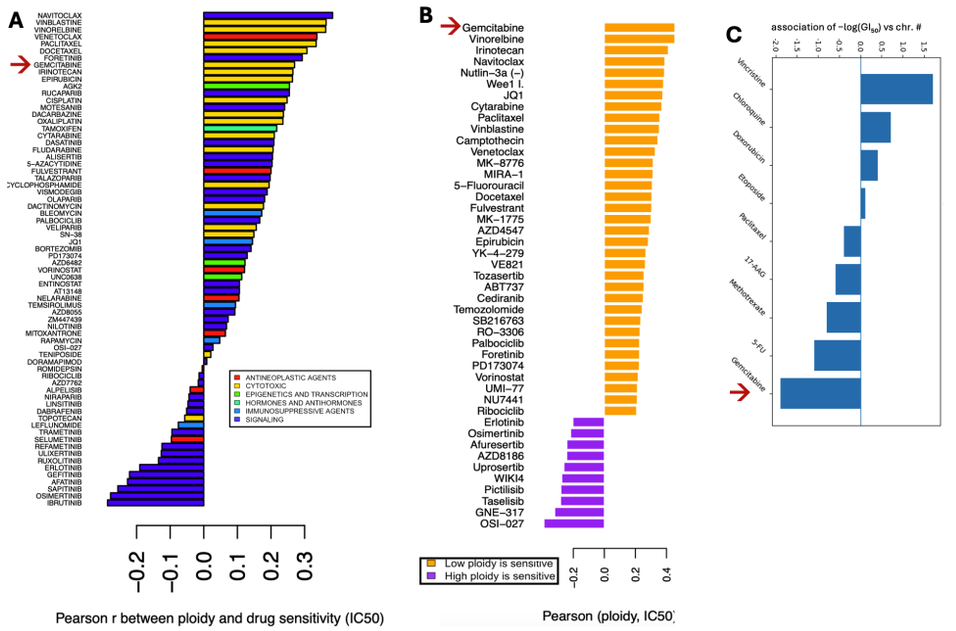

Figure 1. Ploidy predicts gemcitabine response across independent pharmacogenomic datasets. (A) Pearson correlation coefficient between ploidy of a given cell line and IC50 of that cell line is shown for multiple drugs administered to Breast Adenocarcinoma (BRCA). Data source: "Genomics of Drug Sensitivity in Cancer" database (GDSC) [25]). (B) Ploidy of 41 breast cancer cell lines correlates with their response to 46 drugs. Figure taken from [8]. Data source: CCLE [26]. (C) Independent pharmacogenomic data nominate gemcitabine as low-ploidy selective. In the NCI-60-derived analysis of standard cancer therapies, gemcitabine showed the strongest negative correlation between ploidy and drug sensitivity among the listed standard agents, consistent with preferential

Gemcitabine emerges as a candidate low-ploidy-selective cytotoxic agent in breast cancer

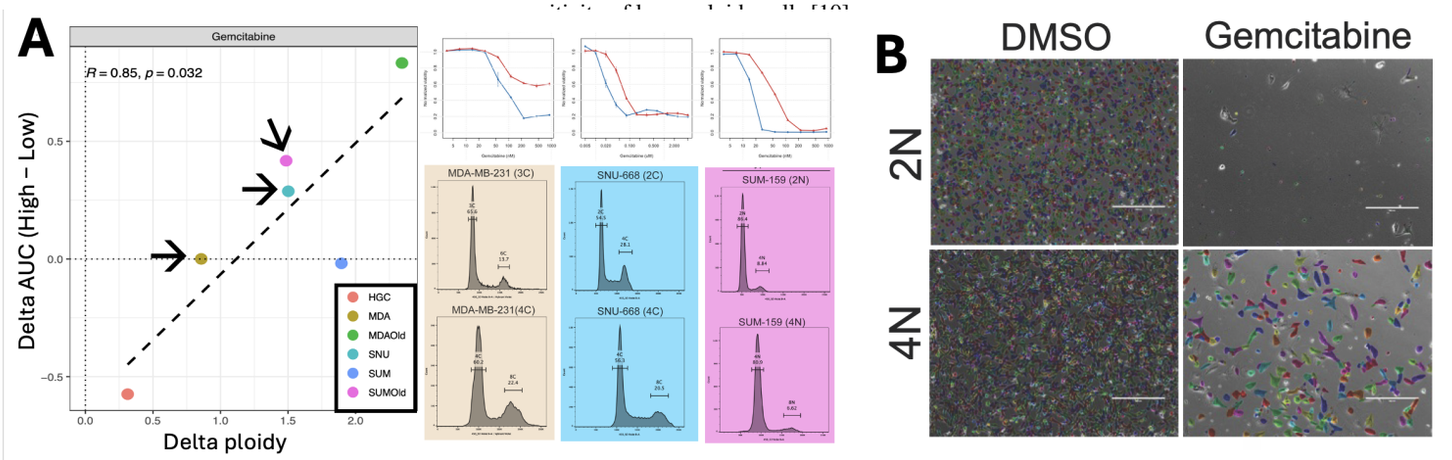

Figure 2. High-ploidy cells are Gemcitabine-resistant. (**A**) Across six low- versus high-ploidy isogenic pairs, the change in ploidy strongly predicts the change in gemcitabine response (left). Right: Drug response curves and flow cytometric DNA content analysis of three representative isogenic pairs (marked by arrows in the left plot). (**B**) Live-cell imaging of Gemcitabine treated near-2N and near-4N isogenic SUM-159 cells.

To move from broad drug classes to a specific therapeutic candidate, we next asked whether any individual cyto-

toxic agents showed consistent ploidy-associated response patterns across independent pharmacogenomic datasets. Gemcitabine emerged as a particularly strong candidate in this analysis. In GDSC breast cancer cell lines, higher ploidy was associated with reduced gemcitabine sensitivity (Fig. 1A). This relationship was further supported by independent analyses of breast cancer cell lines and standard anticancer agents from other pharmacogenomic resources, which likewise identified gemcitabine as preferentially active in lower- ploidy cells (Fig. 1B,C). Together, these orthogonal datasets nominate gemcitabine as a robust low-ploidy-selective cytotoxic agent and motivated direct experimental testing in controlled isogenic systems.

Isogenic cell systems confirm that high-ploidy cells are gemcitabine-resistant

We have established a robust experimental panel consisting of four isogenic lineage-pairs derived from three cancer cell lines (Fig. 2A). Each pair comprises a low-ploidy (range 2 - 3.5) and a high-ploidy counterpart (range 4 - 5.2). These pairs exhibit significant genomic divergence, with ploidy differences ranging between 0.9 and 2.6 haploid genome equivalents. We ensured isogenic lines maintained a differential chromosome number through more than 5 passages. This diverse panel allowed us to decouple the phenotypic effects of increased ploidy from the specific method of its acquisition.

Across SNU-668, SUM-159, and MDA-MB-231 isogenic systems, the higher-ploidy derivatives were consistently less sensitive to gemcitabine across the dose range producing robust cytotoxicity (Fig. 2A).

To investigate the cellular basis of this ploidy-associated resistance in greater detail, we performed high-temporal-resolution live-cell imaging in matched near-2N and near-4N SUM-159 cells (Fig. 2B), together with PKPD profiling of intracellular dFdCTP in the same ploidy states. These experiments showed that, although 4N cells accumulated greater levels of dFdCTP and had similar deactivation trajectories (Fig. 3B), they showed delayed and reduced cytotoxicity relative to near-2N isogenic cells (Fig. 3C). This motivated a joint PKPD/live-dead modeling framework to distinguish differences in intracellular drug exposure from differences in the timing and potency of downstream cytostatic and cytotoxic responses.

despite measurable intracellular formation of the active metabolite in both cell states and had similar deactivation trajectories (Fig. 3B), high-ploidy cells

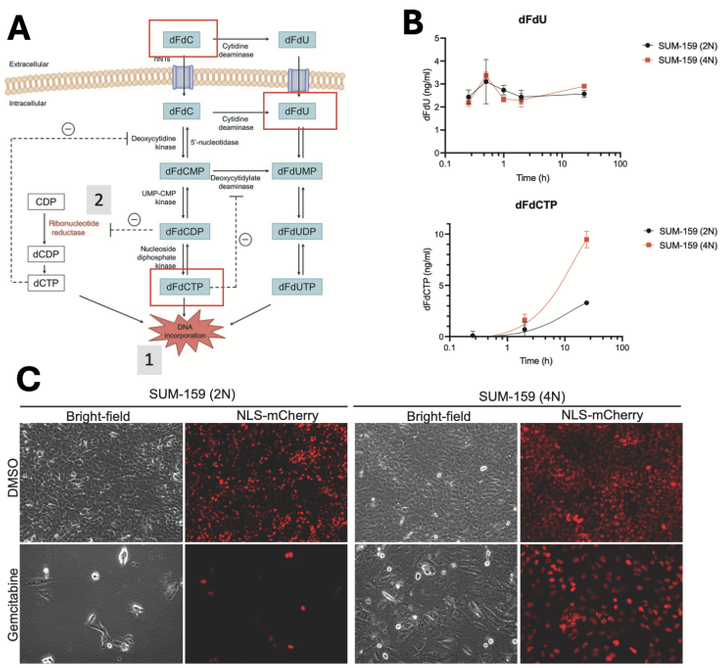

Figure 3. Gemcitabine metabolism, intracellular dFdCTP accumulation, and ploidy-dependent response in SUM-159 cells. (A) Schematic of gemcitabine (dFdC) uptake and metabolism. Extracellular dFdC enters cells and can be phosphorylated through the deoxycytidine salvage pathway to dFdCMP, dFdCDP, and dFdCTP, the active triphosphate metabolite that can be incorporated into DNA. Gemcitabine metabolites can also be deaminated to dFdU species, and dFdCDP inhibits ribonucleotide reductase, thereby perturbing endogenous deoxynucleotide synthesis. **(B)** Time-resolved measurements of dFdU and dFdCTP in matched SUM-159 near-diploid (2N) and near-tetraploid (4N) cells following gemcitabine exposure. dFdU levels were broadly similar between 2N and 4N cells, whereas dFdCTP accumulated to higher levels in 4N cells. **(C)** Representative bright-field and NLS-mCherry images of SUM-159 2N and 4N cells treated with DMSO or gemcitabine. Gemcitabine caused marked loss of viable/nuclear signal in 2N cells, whereas 4N cells retained more cells and nuclear signal under the same treatment condition, consistent with relative gemcitabine resistance despite detectable active-metabolite accumulation.

Gemcitabine-induced death is delayed, with longer inferred delay in high-ploidy cells

We first asked whether time-resolved live/dead imaging data could be explained by a compact model in which gemcitabine response is driven by intracellular dFdCTP exposure. To this end, we developed a delay-aware live/dead compartment model in which intracellular dFdCTP exposure modulates live-cell growth immediately while feeding a latent transit chain that converts drug-induced damage into delayed cell death (Fig. 4A; Supplementary methods). We fit the model jointly to alive/dead counts across gem-

citabine doses, replicates, and ploidy states. The default model used an intracellular dFdCTP signal surface derived from the PKPD measurements, an empirical dose-response correction consisting of a ploidy-specific power-law term and a shared Hill gate, immediate cytostasis, delayed cytotoxicity through a transit chain, and drug-independent baseline and confluence-associated death.

Table 1. Best-fit parameters for the default gemcitabine live/dead model.

Parameter	Units	Brief definition	2N	4N
r	day^{-1}	Max. proliferation rate of live cells	1.25	1.78
K	cells (or live objects)	Carrying capacity	25,358	20,512
k_{tr}	day^{-1}	Transit rate governing delay from effective dFdCTP exposure to death signal	6.84	2.82
n_{tr}	dimensionless	Number of transit compartments in the linear-chain delay model	5	5
k_{kill}	$\text{day}^{-1}(\mu\text{M dFdCTP})^{-1}$	Cytotoxic potency per unit delayed intracellular drug signal	217.3	129.9
k_{clear}	day^{-1}	Clearance/disappearance rate of observed dead cells	0.152	0.062
k_{cyto}	$(\mu\text{M dFdCTP})^{-1}$	Cytostatic potency controlling suppression of proliferation by intracellular drug	8041	1163
β	dimensionless	Dose-scaling exponent: administered gemcitabine –> intracellular drug signal	0.253	0.488
μ_{base}	day^{-1}	Baseline drug-independent death hazard	0.117	0.017
μ_{conf}	day^{-1}	Confluence-associated death hazard scale	0.051	0.054

The fitted model reproduced the major features of the live and dead object trajectories across both 2N and 4N cells (Fig. **??**). In particular, the model captured the high-dose decline in live cells, the delayed accumulation of dead objects, and the qualitative separation between low-dose, intermediate-dose, and high-dose gemcitabine responses. The best fit was obtained with $n_{\text{tr}} = 5$ transit compartments across 8,780 alive/dead observations (Table 1; Supplementary Table 2).

The transit-chain component provided an empirical estimate of the delay between effective intracellular dFdCTP exposure and observed death. For the best model, $n_{\text{tr}} = 5$. The fitted transit rates were $k_{\text{tr},2N} = 6.84\ \text{day}^{-1}$ and $k_{\text{tr},4N} = 2.82\ \text{day}^{-1}$, corresponding to approximate mean delays $n_{\text{tr}}/k_{\text{tr}}$ of 0.73 days (~ 17.5 hours) for 2N cells and 1.77 days (~ 42.5 hours) for 4N cells. Thus, although the model does not explicitly track cell-cycle states, it infers a substantially longer delay from effective gemcitabine activity to death commitment in 4N cells.

The fitted potency parameters also differed by ploidy. The 2N cells had higher fitted drug-induced cytotoxic potency ($k_{\text{kill},2N} = 217.3$) than 4N cells ($k_{\text{kill},4N} = 129.9$). Similarly, immediate cytostatic potency was larger in 2N cells ($k_{\text{cyto},2N} = 8041$) than in 4N cells ($k_{\text{cyto},4N} = 1163$). Together, these results indicate that the fitted model attributes the stronger gemcitabine sensitivity of 2N cells to both stronger immediate proliferation suppression and stronger delayed death, whereas 4N cells exhibit a slower delayed-death timescale (Fig. 4D; Table 1).

The initial PK-derived dFdCTP signal surface was insufficient by itself to align the lowest and intermediate gemcitabine doses. The best model therefore included an empirical effective dose-response correction consisting of a ploidy-specific power-law term and a shared Hill gate (Eq. (1)). The fitted Hill gate had $EC_{50} = 0.0185\ \mu\text{M}$ and Hill coefficient $h = 2.69$, placing the inferred activation threshold in the dose range where the live/dead trajectories transition from near-control behavior to substantial response. Overall, the fitted correction suppressed effective drug action at the lowest doses, amplified the intermediate response range, and compressed higher doses relative to the reference dose (Table 3). Here, the ploidy-specific terms imply that 2N cells map the same administered gemcitabine dose to a stronger effective intracellular drug-action signal than 4N cells, particularly in the low-to-intermediate dose range. We interpret this as evidence for a thresholded, nonlinear, and ploidy-dependent mapping from administered gemcitabine exposure to effective intracellular response.

To determine whether ploidy alters the conversion of intracellular gemcitabine exposure into downstream replication-stress signaling, we measured checkpoint activation 24h after gemcitabine treatment in matched near-2N and near-4N SUM-159

cells. Gemcitabine induced phosphorylation of CHK1, and to a lesser extent CHK2, at lower administered doses in 2N cells than in 4N cells (Fig. 4E). Because CHK1 is a canonical effector of ATR-dependent replication-stress signaling, these data indicate that low-ploidy cells activate the replication-stress/DNA-damage checkpoint at lower gemcitabine doses. Together with intracellular dFdCTP measurements and live/dead imaging, this supports a model in which high-ploidy resistance reflects attenuated conversion of gemcitabine exposure into checkpoint activation and delayed cytotoxicity.

To determine whether attenuated checkpoint activation could reflect reduced upstream nucleotide-pathway perturbation rather than only decreased checkpoint sensitivity to damage, we performed untargeted metabolomics 24 hours after gemcitabine exposure to ask whether low- and high-ploidy cells differed in the upstream metabolic consequences of treatment, focusing on nucleotide-pathway metabolites detected in the assay. Gemcitabine produced a marked reduction. Gemcitabine produced a marked reduction in dCMP abundance in 2N cells, whereas 4N cells showed a significantly smaller fold-change (Fig. 4F). Because dCMP lies in the deoxycytidine salvage pathway that overlaps with gemcitabine activation, this result suggests that high-ploidy cells experience a milder perturbation of deoxycytidine nucleotide metabolism at the same administered dose. Together with the lower pCHK1/pCHK2 induction in 4N cells, these data support an upstream metabolic contribution to the attenuated replication-stress response in high-ploidy cells.

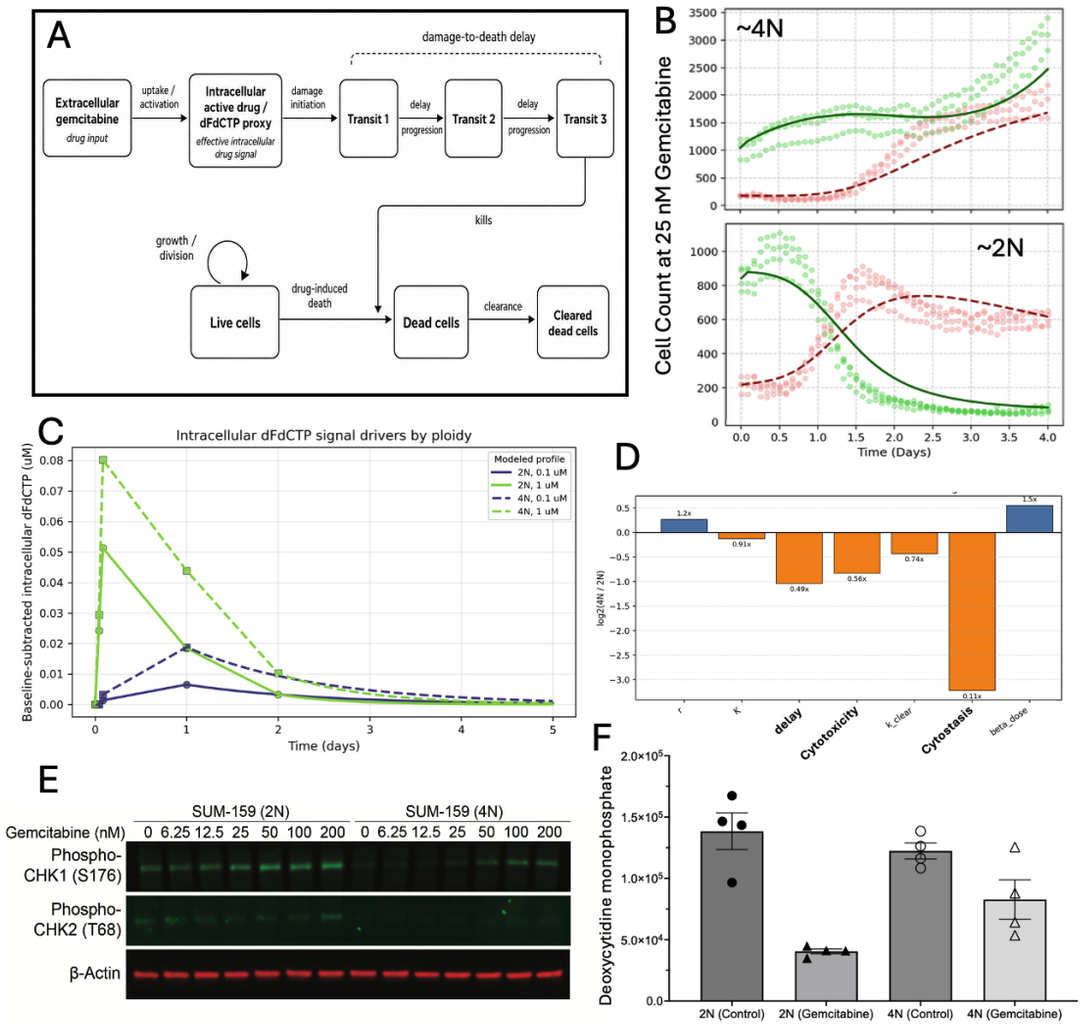

Figure 4. Ploidy reshapes gemcitabine metabolism, checkpoint activation, and delayed cytotoxicity (A) Delay-aware gemcitabine live/dead model. Extracellular gemcitabine is converted into an effective intracellular active-drug signal (dFdCTP), which feeds a latent transit chain representing the delay between damage initiation and observed cell death. The terminal transit compartment drives gemcitabine-induced conversion of live cells into dead cells, while dead cells are subsequently cleared. (B) Predicted and observed live-dead dynamics of isogenic near-2N and near-4N cells treated with Gemcitabine. Only 1 of 10 doses is shown. (C) Intracellular dFdCTP signal drivers used for the gemcitabine live/dead model. Baseline-subtracted dFdCTP measurements and the corresponding PK-derived signal curves are shown for 2N and 4N cells at the calibrated gemcitabine reference doses. Solid lines denote 2N profiles and dashed lines denote 4N profiles; colors indicate administered gemcitabine dose. These ploidy-specific dFdCTP signal surfaces provide the upstream drug exposure input used for cytostasis and delayed cytotoxicity in the live/dead model. (D) Ploidy-associated parameter differences. Bars show $\log_2$ fold-changes comparing 4N to 2N fitted parameter values. Negative values indicate lower fitted values in 4N cells. The 4N fit shows a lower transit rate, corresponding to a longer inferred delay from effective dFdCTP exposure to death commitment. (E) Gemcitabine induces stronger low-dose checkpoint activation in 2N cells. Immunoblotting shows higher phospho-CHK1, and to a lesser extent phospho-CHK2, at lower gemcitabine doses in 2N compared with 4N cells. (F) High-ploidy cells show milder gemcitabine-induced perturbation of dCMP abundance. At 24 hours, gemcitabine causes a larger fold-change in deoxycytidine monophosphate levels in 2N cells, whereas 4N cells show significantly less dCMP perturbation.

Discussion

Our results establish that ploidy is associated with both the magnitude and timing of gemcitabine response. Across public pharmacogenomic datasets, gemcitabine repeatedly emerged as a low-ploidy-selective cytotoxic agent. In matched isogenic systems, higher-ploidy cells were less sensitive to gemcitabine, and in the SUM-159 live/dead model this relative resistance was associated with weaker fitted cytostatic and cytotoxic potency together with a substantially longer delay from effective intracellular dFdCTP exposure to observed death. Thus, the current data support a parsimonious interpretation in which ploidy reshapes gemcitabine response through altered effective drug-action mapping and delayed execution of cell death.

The immunoblotting data provide a mechanistic anchor for the model-inferred ploidy-dependent potency shift. Gemcitabine induced stronger phosphorylation of CHK1, and to a lesser extent CHK2, at lower doses in 2N than in 4N cells, consistent with stronger replication-stress/DNA-damage checkpoint activation in low-ploidy cells at matched administered dose. However, checkpoint activation can be both a marker of damage and a protective response. Future time-resolved and cell-cycle-resolved measurements will therefore be needed to determine whether 4N cells experience less initial replication stress, delayed checkpoint activation, enhanced fork protection, or greater tolerance of damage carried into mitosis.

The metabolomics data suggest one possible upstream contribution to this phenotype. Although dNTPs were not directly detected, gemcitabine caused a larger reduction in dCMP abundance in 2N cells, whereas 4N cells showed a smaller fold-change. This is consistent with the possibility that high-ploidy cells better maintain cytidine/deoxycytidine nucleotide homeostasis during gemcitabine exposure. This interpretation is also important for evaluating intracellular dFdCTP measurements: because 4N cells are larger, greater total dFdCTP accumulation in 4N cells (Fig. 3B), need not imply greater effective drug pressure per unit DNA, cell volume, replication fork, or competing cytidine nucleotide pool. One plausible explanation is that proliferative high-ploidy cells that have successfully adapted to genome doubling are under selection for stronger nucleotide-homeostasis programs, including larger baseline nucleotide reserves, enhanced de novo pyrimidine synthesis, or greater capacity to buffer salvage-pathway perturbation. Such adaptations would be expected to support replication of a larger genome and may incidentally reduce the effective replication-stress burden imposed by gemcitabine. However, because steady-state dCMP abundance does not directly measure dNTP pools or nucleotide flux, future isotope-tracing and targeted dNTP/dFdCTP measurements will be required to distinguish increased de novo synthesis from altered salvage, catabolism, nucleotide utilization, or scaling effects related to cell size and DNA content.

A second, non-mutually exclusive interpretation is that higher-ploidy cells may also be better able to tolerate the chromosomal consequences of replication-stress-induced missegregation. Under-replicated DNA becomes most dangerous when cells enter mitosis before replication is complete, because unresolved loci can generate ultrafine anaphase bridges, chromatin bridges, acentric fragments, micronuclei, and post-mitotic genome loss [27–29]. In this framework, high ploidy is not expected to be uniquely compatible with upstream pharmacologic resistance mechanisms, which primarily reduce effective intracellular drug burden. Instead, high ploidy is most compatible with downstream resistance mechanisms that require survival after imperfect genome duplication, including tolerance of under-replicated DNA entering mitosis, bridge or micronucleus resolution, senescence or PGCC-like persistence, and viable exit from abnormal mitoses [30–33]. Thus, our results support a model in which gemcitabine resistance can arise not only by reducing the initial replication lesion, but also by increasing the probability that cells survive the chromosomal damage produced when replication stress is carried into mitosis.

Methods

Pharmacogenomic analysis of ploidy-associated drug classes

We integrated drug-sensitivity data from GDSC [25] with cell-line ploidy estimates from CellPassports [34] . Drugs were assigned to six functional categories using DrugBank [35] and PubChem [36] CYTOTOXIC, EPIGENETICS AND TRANSCRIPTION, IMMUNOSUPPRESSIVE AGENTS, SIGNALING, ANTINEOPLASTIC AGENTS, and HORMONES AND ANTIHORMONES. For each drug, we calculated the Pearson correlation coefficient between cell-line ploidy and IC50 across matched cell lines. We then tested for enrichment of drug classes among compounds with strong positive or negative ploidy-response correlations using the `enrichment()` function from the R package `EnrichIntersect`.

Cell viability and cell death assay

Cell viability assays were carried out using the IncuCyte live-cell imaging system (Sartorius). Briefly, 2N and 4N SUM-159-NLS-mCherry cells were plated in four replicates in 96-well plates (Falcon, Corning, New York, USA) at a density of 1000 cells per well and treated with a 10-point 2X serial dilutions of gemcitabine within the concentration range of 0 and 800 nM. Sytox Deep Red (S11381, ThermoFisher Scientific) nucleic acid stain was also added to monitor dead cells. Plates were then incubated in the IncuCyte CO2 incubator for 10 days while four separate images were captured from each well every 2 hours using 10× objective in red, infrared and phase channels. Red object count (ROC) per well was calculated as a measure of viable cells and near-infrared object counts (NOC) per well was calculated as a measure of dead cells when the treatment was performed.

Quantification of Gemcitabine Metabolites by LC–MS/MS

SUM-159 cells were seeded and treated with vehicle or gemcitabine for the indicated time points up to 48 h. For each condition, $2 \times 10\hat{6}$ cells were collected, pelleted by centrifugation at 1,000 rpm for 5 min at 4°C, washed with cold PBS, flash frozen in liquid nitrogen, and stored at 80°C until metabolite extraction. For extraction, frozen cell pellets were resuspended in 500 µL ice-cold methanol and vortexed vigorously. Samples were vortexed again and centrifuged at 16,000 × g for 5 min at 4°C. A total of 700 µL supernatant was transferred to a new 1.5-mL tube and evaporated to dryness at 37°C using a centrifugal evaporator.

Dried extracts were reconstituted in 100 µL of 10 mmol/L ammonium bicarbonate/acetonitrile [35:65, v/v]. After centrifugation at 16,000 × g for 5 min, 70 µL of the supernatant was transferred to LC–MS vials for analysis. Quantification of gemcitabine (dFdC), gemcitabine monophosphate (dFdCMP), gemcitabine diphosphate (dFdCDP), gemcitabine triphosphate (dFdCTP), and the deaminated metabolite 2,2-difluorodeoxyuridine (dFdU) was performed using a Xevo TQ-S micro triple quadrupole mass spectrometer coupled to an ACQUITY UPLC H-Class Bio system (Waters).

Two microliters of each sample were injected onto a SeQuant ZIC-pHILIC column (5 µm, 4.6 × 150 mm; Merck Millipore) maintained under hydrophilic interaction chromatography conditions. The flow rate was 0.5 mL/min. Mobile phase A consisted of 10 mmol/L ammonium bicarbonate with 0.05% ammonium hydroxide, and mobile phase B consisted of acetonitrile. The gradient was as follows: 0–5 min, linear gradient from 65% B to 40% B; 5–7 min, linear gradient to 0% B; 7–9 min, isocratic at 0% B; 9–9.1 min, linear gradient to 65% B; and 9.1–15 min, isocratic at 65% B for column re-equilibration.

Analytes were detected by multiple reaction monitoring in positive-ion mode using nitrogen as the nebulizing and desolvation gas and argon as the collision gas. Source conditions were as follows: ion source temperature, 150°C; desolvation temperature, 550°C; desolvation gas flow, 1,200 L/h; cone gas flow, 110 L/h; and capillary voltage, 2.0 kV. Representative MRM transitions were monitored using compound-specific cone voltages and collision energies optimized with authentic standards: dFdC, 264.1 > 112.0 (20 V, 15 eV); dFdCMP, 344.0 > 112.0 (20 V, 20 eV); dFdCDP, 424.0 > 112.0 (20 V, 25 eV); dFdCTP, 503.1 > 112.0 (20 V, 35 eV); and dFdU, 265.1 > 113.0 (20 V, 15 eV).

Metabolite abundance was quantified by calculating the peak area ratio of each analyte to its corresponding internal standard. Calibration curves were generated using authentic metabolite standards spiked with matched internal standards and processed in parallel with experimental samples. Metabolite levels were normalized to cell number, and dFdCTP accumulation and dFdU formation were reported relative to time-zero controls, as indicated.

PKPD measurement of intracellular dFdCTP

To construct the intracellular drug-action input for the live/dead model, we used PKPD measurements of gemcitabine metabolites collected for the matched 2N and 4N cell states. The live/dead model was driven by the intracellular active metabolite dFdCTP, rather than by parent gemcitabine concentration. For each ploidy, PKPD sheets corresponding to the main-dose and low-initial-dose gemcitabine conditions were used to define calibrated dFdCTP time courses. The main 2N and 4N PKPD sheets were treated as $1.0\ \mu\mathrm{M}$ gemcitabine reference-dose profiles, whereas the low-initial-gemcitabine 2N and 4N sheets were treated as $0.1\ \mu\mathrm{M}$ reference-dose profiles.

PKPD dFdCTP measurements were reported in ng/mL and converted to μM-equivalent concentrations using the dFdCTP molecular weight,

$$503.1\ \mathrm{ng/nmol}.$$

Because

$$1\ \mathrm{nmol/mL} = 1\ \mu\mathrm{M},$$

the conversion was

$$C_{\mathrm{dFdCTP}}\ (\mu\mathrm{M}) = \frac{C_{\mathrm{dFdCTP}}\ (\mathrm{ng/mL})}{503.1\ \mathrm{ng/nmol}}.$$

The resulting dFdCTP profiles were baseline-subtracted using the first measured time point so that the model input represented treatment-induced intracellular dFdCTP above the initial measured level.

Image analysis

Cell segmentation and classification with HALO

Cell segmentation was achieved by training a single-cell segmentation neural network in Halo-AI platform [37]. At the beginning, a training dataset was collected by selecting a subsample of images from the data. Two main selection criteria were considered during the image sampling. First, the training set must have representative images from both 2N and 4N cells. Second, multiple images were sampled from different time points for each cell type 2N and 4N to ensure the capture of cell change over time during the training process. After the selection of train set, nucleus of cells was labeled using Halo built-in labeling tools. Finally, the training process was performed until all cells are accurately segmented. Another object classifier was trained on the top of the cell segmentation classifier results to classify each segmented cell to either dead, alive or transitional cell. At the beginning, cells are labeled either dead or alive by tracking the cells over the time and by observing changes in their nuclei. The object classifier was trained iteratively until the cell were classified correctly.

Western blotting

Cells were seeded in 6-well plates at $2 \times 10\hat{5}$ cells per well and treated with the indicated compounds at the indicated concentrations. Forty-eight hours after treatment, culture medium was aspirated and cells were washed once with cold PBS. Cells were lysed in ice-cold RIPA buffer containing 50 mmol/L Tris-HCl pH 8.0, 150 mmol/L NaCl, 1% NP-40, 0.1% SDS, and 0.5% sodium deoxycholate, supplemented with protease and phosphatase inhibitor cocktails. Lysates were clarified by centrifugation at 14,000 × g for 10–15 min at 4°C, and protein concentrations were determined using the DC Protein Assay (Bio-Rad, 500-0111).

Equal amounts of protein were resolved by SDS-PAGE and transferred to low-fluorescence nitrocellulose membranes. Membranes were blocked in LI-COR Intercept Blocking Buffer for 1 h at room temperature and incubated overnight at 4°C with primary antibodies against phospho-CHK1, phospho-CHK2, and β-actin as an internal loading control. After washing with PBS-T, membranes were incubated for 1 h at room temperature with species-appropriate IRDye 680RD- or IRDye 800CW-conjugated secondary antibodies protected from light. Membranes were washed again with PBS-T followed by PBS and imaged using a LI-COR Odyssey infrared imaging system.

Untargeted Metabolomics

Untargeted global metabolomics was performed on samples from SUM-159 cells via ultra-high performance liquid chromatography/tandem mass spectroscopy methods, including: 1) acidic positive ion conditions, one chromatographically optimized for more hydrophilic compounds, the other chromatographically optimized for more hydrophobic compounds; 2) basic negative ion optimized conditions; and 3) negative ionization. In total 474 compounds were detected in the samples. Raw signals were median normalized and missing values were imputed using the half minimum detected value for that compound.

Funding

This work was supported by the NCI grants 1R03CA259873-01A1, 1R37CA266727-01A1 and 1R21CA269415-01A1 awarded to N. Andor. The funders had no role in study design, data collection and analysis, decision to publish, or preparation of the manuscript.

References

[1] Saioa López, Emilia L. Lim, Stuart Horswell, Kerstin Haase, Ariana Huebner, Michelle Dietzen, Thanos P. Mourikis, Thomas B. K. Watkins, Andrew Rowan, Sally M. Dewhurst, Nicolai J. Birkbak, Gareth A. Wilson, Peter Van Loo, Mariam Jamal-Hanjani, Charles Swanton, Mariam Jamal-Hanjani, Gareth A. Wilson, Nicolai J. Birkbak, Thomas B. K. Watkins, Nicholas McGranahan, Christopher Abbosh, Rachel Rosenthal, Yin Wu, Mickael Escudero, Aengus Stewart, Andrew Rowan, Jacki Goldman, Selvaraju Veeriah, Marcin Skrzypski, Robert E. Hynds, Andy Georgiou, Mariana Werner Sunderland, James Reading, Sergio Quezada, Karl Peggs, Teresa Marafioti, Peter Van Loo, John A. Hartley, Richard Kevin Stone, Tamara Denner, Emma Nye, Sophia Ward, Emilia L. Lim, Stefan Boeing, Maria Greco, Maise Al-Bakir, Kevin Litchfield, Pat Gorman, Helen L. Lowe, Leah Ensell, Victoria Spanswick, Angeliki Karamani, David Moore, Dhruva Biswas, Maryam Razaq, Jerome Nicod, Stephan Beck, Ariana Huebner, Michelle Dietzen, Cristina Naceur-Lombardelli, Mita Afroza Akther, Haoran Zhai, Nnennaya Kannu, Elizabeth Manzano, Clare Puttick, Katey Enfield, Emma Colliver, Brittany Campbell, Supreet Kaur Bola, Ehsan Ghorani, Marc Robert De Massy, Elena Hoxha, Emine Hatipoglu, Stephanie Ogwuru, Benny Chain, Jason Lester, Fiona Morgan, Malgorzata Kornaszewska, Richard Attanoos, Haydn Adams, Helen Davies, Dean Fennell, John Le Quesne, Apostolos Nakas, Sridhar Rathinam, William Monteiro, Hilary Marshall, Louise Nelson, Kim Ryanna, Alan Dawson, Mohamad Tuffail, Amrita Bajaj, Jan Brozik, Mark R. Lovett, Jacqui A. Shaw, Joan Riley, Lindsay Primrose, Luke Martinson, Nicolas Carey, Girija Anand, Sajid Khan, Gillian Price, Marianne Nicolson, Keith Kerr, Shirley Palmer, Hardy Remmen, Joy Miller, Keith Buchan, Mahendran Chetty, Lesley Gomersall, Sara Lock, Kayleigh Gilbert, Babu Naidu, Gerald Langman, Andrew Robinson, Hollie Bancroft, Amy Kerr, Salma Kadiri, Charlotte Ferris, Gary Middleton, Madava Djearaman, Akshay Patel, Yvonne Summers, Raffaele Califano, Paul Taylor, Rajesh Shah, Piotr Krysiak, Kendadai Rammohan, Eustace Fontaine, Richard Booton, Matthew Evison, Phil Crosbie, Stuart Moss, Juliette Novasio, Leena Joseph, Paul Bishop, Anshuman Chaturvedi, Helen Doran, Felice Granato, Vijay Joshi, Angela leek, Phil Harrison, Katrina Moore, Rachael Waddington, Fiona Blackhall, Jane Rogan, Elaine Smith, Katie Baker, Mathew Carter, Lynsey Priest, Matthew G. Krebs, C. R. Lindsay, Fabio Gomes, Angeles Montero, Caroline Dive, Ged Brady, Dominic G. Rothwell, Francesca Chemi, Jonathan Tugwood, Jackie Pierce, David Lawrence, Martin Hayward, Nikolaos Panagiotopoulos, Robert George, Davide Patrini, Mary Falzon, Elaine Borg, Reena Khiroya, Crispin Hiley, Asia Ahmed, Magali Taylor, Junaid Choudhary, Penny Shaw, Sam M. Janes, Martin Forster, Tanya Ahmad, Siow Ming Lee, Javier Herrero, Dawn Carnell, Ruheena Mendes, Jeremy George, Neal Navani, Dionysis Papadatos-Pastos, Marco Scarci, Roberto Salgado, Elisa Bertoja, Robert C. M. Stephens, Emilie Martinoni Hoogenboom, James W. Holding, Steve Bandula, Hugo Aerts, Roland Schwarz, Zoltan Szallasi, Istvan Csabai, Miklos Diossy, Mairead MacKenzie, Maggie Wilcox, Allan Hackshaw, Yenting Ngai, Abigail Sharp, Cristina Rodrigues, Oliver Pressey, Sean Smith, Nicole Gower, Harjot Dhanda, Christian Ottensmeier, Serena Chee, Benjamin Johnson, Aiman Alzetani, Emily Shaw, Eric Lim, Paulo De Sousa, Simon Jordan, Alexandra Rice, Hilgardt Raubenheimer, Harshil Bhayani, Morag Hamilton, Lyn Ambrose, Anand Devaraj, Hema Chavan, Sofina Begum, Aleksander Mani, Daniel Kaniu, Mpho Malima, Sarah Booth, Andrew G. Nicholson, Nadia Fernandes, Jessica E. Wallen, Pratibha Shah, Kelvin Lau, Michael Sheaff, Peter Schmid, Louise Lim, John Conibear, Veni Ezhil, Vineet Prakash, Sarah Danson, Jonathan Bury, John Edwards, Jennifer Hill, Sue Matthews, Yota Kitsanta, Jagan Rao, Sara Tenconi, Laura Socci, Kim Suvarna, Faith Kibutu, Patricia Fisher, Robin Young, Joann Barker, Michael Shackcloth, John Gosney, Sarah Feeney, Julius Asante-Siaw, Teresa Light, Tracey Horey, Dionysis Papadatos-Pastos, Peter Russell, Kevin G. Blyth, Craig Dick, Andrew Kidd, Alan Kirk, Mo Asif, John Butler, Rocco Bilanca, Nikos Kostoulas, Charles Swanton, Nicholas McGranahan, and TRACERx Consortium. Interplay between whole-genome doubling and the accumulation of deleterious alterations in cancer evolution. 52(3):283–293. Read_Status: New Read_Status_Date: 2025-11-22T17:34:32.503Z.

[2] Sergi Elizalde, Ashley M. Laughney, and Samuel F. Bakhoum. A markov chain for numerical chromosomal instability in clonally expanding populations. 14(9):e1006447.

[3] Jason M. Sheltzer, Julie H. Ko, John M. Replogle, Nicole C. Habibe Burgos, Erica S. Chung, Colleen M. Meehl, Nicole M. Sayles, Verena Passerini, Zuzana Storchova, and Angelika Amon. Single-chromosome gains commonly function as tumor suppressors. 31(2):240–255.

[4] Sarah L. Thompson and Duane A. Compton. Proliferation of aneuploid human cells is limited by a p53-dependent mechanism. 188(3):369–381.

[5] Stefano Santaguida, Amelia Richardson, Divya Ramalingam Iyer, Ons M'Saad, Lauren Zasadil, Kristin A. Knouse, Yao Liang Wong, Nicholas Rhind, Arshad Desai, and Angelika Amon. Chromosome mis-segregation generates cell cycle-arrested cells with complex karyotypes that are eliminated by the immune system. 41(6):638–651.e5.

[6] Alain D. Silk, Lauren M. Zasadil, Andrew J. Holland, Benjamin Vitre, Don W. Cleveland, and Beth A. Weaver. Chromosome missegregation rate predicts whether aneuploidy will promote or suppress tumors. 110(44):E4134–E4141.

[7] Richard J. Beck, Tao Li, and Noemi Andor. ALFA-k: Local adaptive mapping of karyotype fitness landscapes. Read_Status: New Read_Status_Date: 2026-01-15T18:28:59.199Z.

[8] Gregory J. Kimmel, Mark Dane, Laura M. Heiser, Philipp M. Altrock, and Noemi Andor. Integrating mathematical modeling with high throughput imaging explains how polyploid populations behave in nutrient-sparse environments. 80(22):5109–5120. Read_Status: New Read_Status_Date: 2026-05-31T21:51:37.113Z.

[9] Hee-Sheung Lee, Nicholas C. O. Lee, Natalay Kouprina, Jung-Hyun Kim, Alex Kagansky, Susan Bates, Jane B. Trepel, Yves Pommier, Dan Sackett, and Vladimir Larionov. Effects of anticancer drugs on chromosome instability and new clinical implications for tumor-suppressing therapies. 76(4):902–911.

[10] Alka Choudhary, Brittany Zachek, Robert F. Lera, Lauren M. Zasadil, Amber Lasek, Ryan A. Denu, Hyunjung Kim, Craig Kanugh, Jennifer J. Laffin, Josephine M. Harter, Kari B. Wisinski, Sandeep Saha, Beth A. Weaver, and Mark E. Burkard. Identification of selective lead compounds for treatment of high-ploidy breast cancer. 15(1):48–59. Read_Status: New Read_Status_Date: 2026-01-15T19:29:31.758Z.

[11] Therese Wilhelm, Anna-Maria Olziersky, Daniela Harry, Filipe De Sousa, Helène Vassal, Anja Eskat, and Patrick Meraldi. Mild replication stress causes chromosome mis-segregation via premature centriole disengagement. 10(1). Read_Status: New Read_Status_Date: 2026-05-31T22:56:15.308Z.

[12] Ryan Montano, Nadeem Khan, Huagang Hou, John Seigne, Marc S. Ernstoff, Lionel D. Lewis, and Alan Eastman. Cell cycle perturbation induced by gemcitabine in human tumor cells in cell culture, xenografts and bladder cancer patients: implications for clinical trial designs combining gemcitabine with a chk1 inhibitor. 8(40):67754–67768. Read_Status: New Read_Status_Date: 2026-01-27T20:29:28.069Z.

[13] Won-Kyu Lee, Jason J. Han, Bong-Suk Jin, Doo Wan Boo, and Yeon Gyu Yu. Functional reconstitution of the human serotonin receptor 5-HT6 using synthetic transmembrane peptides. 390(3):815–820. Read_Status: New Read_Status_Date: 2026-05-31T22:56:05.779Z.

[14] Hai Yang, Bin Liu, Dongxue Liu, Zhirong Yang, Shuman Zhang, Pengyan Xu, Yuming Xing, Isabella Kutschick, Susanne Pfeffer, Nathalie Britzen-Laurent, Robert Grützmann, and Christian Pilarsky. Genome-wide CRISPR screening identifies DCK and CCNL1 as genes that contribute to gemcitabine resistance in pancreatic cancer. 14(13):3152. Read_Status: New Read_Status_Date: 2026-05-31T22:56:19.561Z.

[15] Qiangsheng Hu, Yi Qin, Jinfeng Xiang, Wensheng Liu, Wenyan Xu, Qiqing Sun, Shunrong Ji, Jiang Liu, Zheng Zhang, Quanxing Ni, Jin Xu, Xianjun Yu, and Bo Zhang. dCK negatively regulates the NRF2/ARE axis and ROS production in pancreatic cancer. 51(4). Read_Status: New Read_Status_Date: 2026-05-31T22:56:13.517Z.

[16] Congjun Zhang, Shuangyan Ou, Yuan Zhou, Pei Liu, Peiying Zhang, Ziqian Li, Ruocai Xu, and Yuqiang Li. m6a methyltransferase METTL14-mediated upregulation of cytidine deaminase promoting gemcitabine resistance in pancreatic cancer. 11. Read_Status: New Read_Status_Date: 2026-05-31T22:56:17.688Z.

[17] Melanie S. Patzak, Vijayalakshmi Kari, Shilpa Patil, Feda H. Hamdan, Robert G. Goetze, Marius Brunner, Jochen Gaedcke, Julia Kitz, Duncan I. Jodrell, Frances M. Richards, Christian Pilarsky, Robert Gruetzmann, Petra Rümmele, Thomas Knösel, Elisabeth Hessmann, Volker Ellenrieder, Steven A. Johnsen, and Albrecht Neesse. Cytosolic 5-nucleotidase 1a is overexpressed in pancreatic cancer and mediates gemcitabine resistance by reducing intracellular gemcitabine metabolites. 40:394–405. Read_Status: New Read_Status_Date: 2026-05-31T22:56:15.308Z.

[18] Tomotaka Kato, Hiroaki Ono, Mikiya Fujii, Keiichi Akahoshi, Toshiro Ogura, Kosuke Ogawa, Daisuke Ban, Atsushi Kudo, Shinji Tanaka, and Minoru Tanabe. Cytoplasmic RRM1 activation as an acute response to gemcitabine treatment is involved in drug resistance of pancreatic cancer cells. 16(6):e0252917. Read_Status: New Read_Status_Date: 2026-05-31T22:56:17.688Z.

[19] Hiroaki Ono, Yoshiki Murase, Hironari Yamashita, Tomotaka Kato, Daisuke Asano, Yoshiya Ishikawa, Shuichi Watanabe, Hiroki Ueda, Keiichi Akahoshi, Kosuke Ogawa, Atsushi Kudo, Yoshimitsu Akiyama, Shinji Tanaka, and Minoru Tanabe. RRM1 is mediated by histone acetylation through gemcitabine resistance and contributes to invasiveness and ECM remodeling in pancreatic cancer. 62(4). Read_Status: New Read_Status_Date: 2026-05-31T22:56:22.106Z.

[20] Qianfan Liu, Chunzhuo Song, Junjun Li, Meng Liu, Liyue FU, Jiuliang Jiang, Zhirui Zeng, and Haitao Zhu. E2f2 enhances the chemoresistance of pancreatic cancer to gemcitabine by regulating the cell cycle and upregulating the expression of RRM2. 39(9). Read_Status: New Read_Status_Date: 2026-05-31T22:56:19.561Z.

[21] Siang-Boon Koh, Aurélie Courtin, Richard J. Boyce, Robert G. Boyle, Frances M. Richards, and Duncan I. Jodrell. CHK1 inhibition synergizes with gemcitabine initially by destabilizing the DNA replication apparatus. 75(17):3583–3595. Read_Status: New Read_Status_Date: 2026-05-31T22:56:09.615Z.

[22] N.V. Rajeshkumar, Elizabeth De Oliveira, Niki Ottenhof, James Watters, David Brooks, Tim Demuth, Stuart D. Shumway, Shinji Mizuarai, Hiroshi Hirai, Anirban Maitra, and Manuel Hidalgo. MK-1775, a potent wee1 inhibitor, synergizes with gemcitabine to achieve tumor regressions, selectively in p53-deficient pancreatic cancer xenografts. 17(9):2799–2806. Read_Status: New Read_Status_Date: 2026-05-31T22:56:07.648Z.

[23] Leslie A. Parsels, Daria M. Tanska, Joshua D. Parsels, Sonya D. Zabludoff, Kyle C. Cuneo, Theodore S. Lawrence, Jonathan Maybaum, and Meredith A. Morgan. Dissociation of gemcitabine chemosensitization by CHK1 inhibition from cell cycle checkpoint abrogation and aberrant mitotic entry. 15(5):730–739.

[24] Scott C. Smith, Aleksandra V. Petrova, Matthew Z. Madden, Hongyan Wang, Yunfeng Pan, Matthew D. Warren, Claire W. Hardy, Dong Liang, Elaine A. Liu, M. Hope Robinson, Soumon Rudra, Jie Wang, Shahrzad Ehdaivand, Mylin A. Torres, Ya Wang, and David S. Yu. A gemcitabine sensitivity screen identifies a role for NEK9 in the replication stress response. 42(18):11517–11527. Read_Status: New Read_Status_Date: 2026-05-31T22:56:07.648Z.

[25] Wanjuan Yang, Jorge Soares, Patricia Greninger, Elena J. Edelman, Howard Lightfoot, Simon Forbes, Nidhi Bindal, Dave Beare, James A. Smith, I. Richard Thompson, Sridhar Ramaswamy, P. Andrew Futreal, Daniel A. Haber, Michael R. Stratton, Cyril Benes, Ultan McDermott, and Mathew J. Garnett. Genomics of drug sensitivity in cancer (GDSC): a resource for therapeutic biomarker discovery in cancer cells. 41:D955–D961.

[26] Mahmoud Ghandi, Franklin W. Huang, Judit Jané-Valbuena, Gregory V. Kryukov, Christopher C. Lo, E. Robert McDonald, Jordi Barretina, Ellen T. Gelfand, Craig M. Bielski, Haoxin Li, Kevin Hu, Alexander Y. Andreev-Drakhlin, Jaegil Kim, Julian M. Hess, Brian J. Haas, François Aguet, Barbara A. Weir, Michael V. Rothberg, Brenton R. Paolella, Michael S. Lawrence, Rehan Akbani, Yiling Lu, Hong L. Tiv, Prafulla C. Gokhale, Antoine de Weck, Ali Amin Mansour, Coyin Oh, Juliann Shih, Kevin Hadi, Yanay Rosen, Jonathan Bistline, Kavitha Venkatesan, Anupama Reddy, Dmitriy Sonkin, Manway Liu, Joseph Lehar, Joshua M Korn, Dale A. Porter, Michael D. Jones, Javad Golji, Giordano Caponigro, Jordan E. Taylor, Caitlin M. Dunning, Amanda L. Creech, Allison C. Warren, James M. McFarland, Mahdi Zamanighomi, Audrey Kauffmann, Nicolas Stransky, Marcin Imielinski, Yosef E. Maruvka, Andrew D. Cherniack, Aviad Tsherniak, Francisca Vazquez,

Jacob D. Jaffe, Andrew A. Lane, David M. Weinstock, Cory M. Johannessen, Michael P. Morrissey, Frank Stegmeier, Robert Schlegel, William C. Hahn, Gad Getz, Gordon B. Mills, Jesse S. Boehm, Todd R. Golub, Levi A. Garraway, and William R. Sellers. Next-generation characterization of the cancer cell line encyclopedia. 569(7757):503–508.

[27] Neil Beeharry, Jerome Rattner, Juliane Caviston, and Tim Yen. Centromere fragmentation is a common mitotic defect of s and g2checkpoint override. 12(10):1588–1597. Read_Status: New Read_Status_Date: 2026-05-31T22:56:07.648Z.

[28] Rahul Bhowmick, Sheroy Minocherhomji, and Ian D. Hickson. RAD52 facilitates mitotic DNA synthesis following replication stress. 64(6):1117–1126. Read_Status: New Read_Status_Date: 2026-05-31T22:56:11.702Z.

[29] Nannan Kong, Zeyuan Liu, and Ying Wai Chan. RIF1 suppresses the formation of single-stranded ultrafine anaphase bridges via protein phosphatase 1. 42(2):112032. Read_Status: New Read_Status_Date: 2026-05-31T22:56:19.561Z.

[30] Yao Song, Tomohisa Baba, and Naofumi Mukaida. Gemcitabine induces cell senescence in human pancreatic cancer cell lines. 477(3):515–519. Read_Status: New Read_Status_Date: 2026-05-31T22:56:09.615Z.

[31] Yushu Ma, Chien-Hung Shih, Jinxiong Cheng, Hsiao-Chun Chen, Li-Ju Wang, Yanhao Tan, Yuan Zhang, Daniel D. Brown, Steffi Oesterreich, Adrian V. Lee, Yu-Chiao Chiu, and Yu-Chih Chen. High-throughput empirical and virtual screening to discover novel inhibitors of polyploid giant cancer cells in breast cancer. 97(10):5498–5506. Read_Status: New Read_Status_Date: 2026-05-31T22:56:22.107Z.

[32] Anastasia Y. Kuznetsova, Katarzyna Seget, Giuliana K. Moeller, Mirjam S. de Pagter, Jeroen A. D. M. de Roos, Milena Dürrbaum, Christian Kuffer, Stefan Müller, Guido J. R. Zaman, Wigard P. Kloosterman, and Zuzana Storchová. Chromosomal instability, tolerance of mitotic errors and multidrug resistance are promoted by tetraploidization in human cells. 14(17):2810–2820.

[33] Ryan J. Quinton, Amanda DiDomizio, Marc A. Vittoria, Kristýna Kotýnková, Carlos J. Ticas, Sheena Patel, Yusuke Koga, Jasmine Vakhshoorzadeh, Nicole Hermance, Taruho S. Kuroda, Neha Parulekar, Alison M. Taylor, Amity L. Manning, Joshua D. Campbell, and Neil J. Ganem. Whole-genome doubling confers unique genetic vulnerabilities on tumour cells. 590(7846):492–497. Read_Status: New Read_Status_Date: 2026-01-15T18:28:59.199Z.

[34] Dieudonne van der Meer, Syd Barthorpe, Wanjuan Yang, Howard Lightfoot, Caitlin Hall, James Gilbert, Hayley E Francies, and Mathew J Garnett. Cell model passports—a hub for clinical, genetic and functional datasets of preclinical cancer models. 47:D923–D929.

[35] Craig Knox, Vivian Law, Timothy Jewison, Philip Liu, Son Ly, Alex Frolkis, Allison Pon, Kelly Banco, Christine Mak, Vanessa Neveu, Yannick Djoumbou, Roman Eisner, An Chi Guo, and David S Wishart. DrugBank 3.0: a comprehensive resource for 'omics' research on drugs. 39:D1035–1041. 00000.

[36] Sunghwan Kim, Jie Chen, Tiejun Cheng, Asta Gindulyte, Jia He, Siqian He, Qingliang Li, Benjamin A Shoemaker, Paul A Thiessen, Bo Yu, Leonid Zaslavsky, Jian Zhang, and Evan E Bolton. PubChem 2023 update. 51:D1373–D1380.

[37] Inc. Indica Labs. HALO image analysis platform and HALO AI.